

Chapter 8

Confocal Fluorescence Microscopy of Interstitial Fluids in Freezing Electrolyte Solutions*

* This chapter is reproduced, with moderate changes, with permission from J. Cheng, C. Soetjpto, M. R. Hoffmann, and A. J. Colussi, *Journal of Physical Chemistry Letters*, **2010**, 1, 374-378. Copyright © 2010, American Chemical Society

8.1 Abstract

The information content of ice core records and the strength of ice-atmosphere interactions depend on the morphology and composition of the fluid films threading polycrystalline ice. Flat ice surfaces separated by pure water always attract by dispersive forces. Thus, these films owe their existence to the presence of impurities and to curvature effects. Electrolyte impurities induce colligative effects, but also adsorb on charged ice surfaces and screen their resulting electrostatic repulsion. Film thickness δ is not therefore a monotonically increasing function of electrolyte concentration as it may be surmised. This possibility is herein demonstrated via time-resolved confocal fluorescence microscopy imaging of the freezing and thawing process of electrolyte solutions doped with a dual-emission pH probe. During freezing of water, the pH probe accumulates into $12 \pm 2 \mu\text{m}$ thick veins embedded in a pristine ice matrix. The ice front advancing into a 1.0 mM NaCl electrolyte solution, in contrast, engulfs the pH probe into small pockets ($< 1 \times 1 \mu\text{m}^2$) distributed over the sample. Together, these observations are consistent with a non-monotonic dependence of δ on ion concentration. The local pH value increases by less than 0.4 units in the interstitial liquid films during freezing of a 0.1 mM NaCl solution, and by over 1.0 units upon subsequent thawing, revealing that the excess negative charge generated by the preferential incorporation of Cl^- over Na^+ into the ice phase is relieved by the seepage of OH^- slowly produced via $\text{H}_2\text{O} \rightarrow \text{H}^+ + \text{OH}^-$. In contrast, preferential incorporation of the NH_4^+ over the Ac^- into ice leads to the acidification of the interstitial liquid films in ice frozen from dilute NH_4Ac solutions.

8.2 Introduction

Most solids exist as polycrystalline aggregates. Their properties, ranging from the rheology and paleography of glacial ice to the reduction of critical current density in high-temperature superconductors¹⁻³ are determined by the composition and geometry of grain boundaries. Gaps among grains arise because advancing planar solid fronts are unstable and bifurcate under the thermal and concentration gradients generated by freezing itself.⁴⁻⁶ They persist within thermally equilibrated (but dynamically arrested)⁷⁻¹⁰ frozen materials because the fractionation of melt components at grain boundaries usually minimizes interfacial free energy. Chemical¹¹⁻¹³ and biological activity¹⁴⁻¹⁶ in snow, ice cores and permafrost actually takes place in microfluids wetting polycrystalline ice grains that contain the solutes and nutrients rejected by the ice matrix.

Ice is notoriously intolerant to impurities, but interstitial fluids are not concentrates of the starting solutions,¹⁷⁻²¹ because molecular isomorphism imposes strong selectivity rules. For example, ammonium (NH_4^+) and fluoride (F^-), being isoelectronic with H_2O and OH^- , respectively, are selectively but marginally (~ 1 out of 10^4) incorporated into the ice matrix over their counterions. This phenomenon generates transient charge imbalances between the solid and the liquid phases during freezing that eventually relax via migration of the intrinsic H^+/HO^- ice carriers.²²⁻²⁶ Preferential incorporation of cations over anions into the ice lattice therefore leads to acidification of the liquid, and vice versa. The local acidity of interstitial fluids determines, for example, whether weak, volatile acids or bases can be exchanged between ice and the gas phase, and whether reactions between dopants are inhibited or catalyzed in frozen media.²⁷⁻³⁴

The equilibrium fluid films that persist at the air/ice interface below the normal melting point have been characterized theoretically and experimentally.^{17,35-39} Only the dihedral angle of water channels along ice grain boundaries is, however, known with any certainty.^{18,21,40-44} Optically transparent polycrystalline ice seems ideally suited to test current views on grain boundary melting¹⁸. Herein we address these issues, and report preliminary results of a time-resolved confocal fluorescence microscopy study of freezing aqueous electrolyte solutions, and their subsequent thawing.

8.3 Experimental Section

C-SNARF-1 (Invitrogen, C1270, see Scheme 8.1) was used as the dual-emission fluorescence pH indicator. A 50 μM stock C-SNARF-1 solution in MilliQ water was prepared and stored frozen at $-20\text{ }^{\circ}\text{C}$ until use. Sodium chloride ($> 99.9\%$ purity; EMD), ammonium acetate ($>99.999\%$ purity; Aldrich), and ammonium sulfate ($> 99.5\%$ purity; EMD) were used as received. 1 M sodium hydroxide solution (VWR), 30% ammonium hydroxide solution (J.T. Baker), 1 M hydrochloric acid (VWR), 1 M sulfuric acid (VWR), $\text{KH}_2\text{PO}_4 \cdot 3\text{H}_2\text{O}$ (AR; Mallinckrodt), and KH_2PO_4 ($>99.7\%$ purity; Mallinckrodt) were used to adjust the pH of the sample solutions as indicated. All solutions were prepared with deionized water (resistivity 18.2 $\text{M}\Omega\text{ cm}$) purified with a Milli-Q ultrapure water system (Millipore).

Temporally and spectrally resolved fluorescence imaging of test solutions was performed with a Zeiss LSM 510 META NLO confocal laser scanning microscope (CLSM) equipped with a programmable PE-120 Peltier cryostage (Linkam). 1.0 μM C-SNARF-1 test solutions were prepared by dilution of the stock solution in water, or in a

binary electrolyte of known concentration, as indicated. Their pH was adjusted prior to freezing by means of acid (basic) solutions containing the same anion (cation) as the selected electrolyte. Fluorescence was acquired from 30 μl samples of the test solutions contained in a cylindrical well (6.0 mm in diameter, 1.0 mm deep) bored into a clear quartz plate, which was tightly clamped to the cryostage lying on the (x, y)-movable plate of the CLSM. A typical freeze-and-thaw cycle involved a temperature program consisting of three consecutive steps: (1) cooling at -10 K min^{-1} from 298 K to 268 K, (2) holding at 268 K for 5 minutes after completion of sample freezing, and (3) warming at 10 K min^{-1} back to 298 K. The actual sample temperature was simultaneously measured with a calibrated type-K thin wire thermocouple immersed in the test solution (Figure 8.1).

The fluorescence emitted by the sample was continuously scanned during the freeze-thaw cycle, which allowed tracking the advancing ice front by adjusting the position of the stage. LD C-Apochromat 40 \times /1.1 W Corr M27 or EC Plan-Neofluar 10 \times /0.3 objective lenses were used to collect images from x-y planes with (512 \times 512) pixels resolution, which corresponds to (225 $\mu\text{m} \times 225 \mu\text{m}$) and (900 $\mu\text{m} \times 900 \mu\text{m}$) frames, respectively. The following instrumental parameters were used unless otherwise specified: $\lambda_{\text{exc}} = 488$ or 514 nm at 50% argon laser output power, 15% transmission; scan speed: 1.0 frame s^{-1} ; pinhole set at 750, corresponding to a z-slice of $< 9.3 \mu\text{m}$ for the 40 \times /1.1 objective; detector gain: 720. The META detector and the Lambda acquisition mode were used to obtain fluorescence emission spectra from 565.1 nm to 650.7 nm with a step size of 10.7 nm. The images were analyzed using Zeiss LSM Image Examiner software.

The pH dependence of C-SNARF-1 fluorescence emissions was independently calibrated with a Perkin Elmer LS 50B luminescence spectrometer. 3.0 mL of 0.2 μ M C-SNARF-1 solutions in 0.05 M $\text{KH}_2\text{PO}_4/\text{K}_2\text{HPO}_4$ buffers contained in square prismatic silica cuvettes were excited at $\lambda_{\text{exc}} = 514$ nm, and emission spectra recorded between 550 and 750 nm. The excitation slit and scan speed were set at 10 and 200 nm min^{-1} , respectively.

8.4 Results and Discussion

The fluorescence emission of C-SNARF-1 as a function of pH was calibrated with the CLSM using 1.0 μ M C-SNARF-1 solutions in 0.05 M $\text{KH}_2\text{PO}_4/\text{K}_2\text{HPO}_4$ buffer at different pH values ranging from 5.6 to 9.2, under different conditions of temperature, C-SNARF-1 concentration, laser intensity, scan speed, and detector gain. The fluorescence emission spectra of C-SNARF-1 show two distinctive emission maxima at $\lambda_1 = 581$ nm and $\lambda_2 = 635$ nm. $R = I(\lambda_1)/I(\lambda_2)$, is the ratio of their corresponding fluorescence intensities. Figure 8.2 shows R vs. pH calibration curves obtained by fitting equation (8.1):

$$\text{pH} = \text{p}K_a + \beta \log \frac{R - R_{\min}}{R_{\max} - R} + \log \frac{I^a}{I^b} \quad (8.1)$$

to CLSM or fluorometer R measurements. $\text{p}K_a$ (C-SNARF-1) = 7.5, R_{\max} and R_{\min} are the maximum and minimum R -values, respectively, and $I(\lambda_1)^a/I(\lambda_2)^b$ is the ratio of $I(\lambda_1)$ in acid to that in base. Ratiometric measurements minimize uneven probe distribution, differences in sample thickness, photobleaching and self-quenching effects.⁴⁵⁻⁴⁶ As long as fluorescence is not oversaturated, calibration curves are also insensitive to sample

concentration and instrumental parameters such as excitation laser intensity, scan speed, and detector gain (See Figure 8.7). Temperature has a minor effect on R vs. pH calibration curves (~ 0.01 pH K^{-1} between 268 and 298 K, see Table 8.1 and Figure 8.6). Other factors, such as ionic strength variations are negligible under present conditions.⁴⁷

Figure 8.1 shows that under a preset cooling ramp of -10.0 K min^{-1} , the sample temperature T_s fell at about -7.9 K min^{-1} down to $T_s \sim 268$ K during step (1), when the electrolyte solution began to freeze, releasing latent heat. T_s remained at ~ 273 K during freezing, before cooling to 265 K for the rest of step (2). We found that cooling ramp settings affect the velocity of the ice front rather than T_s during step (2). As the ice front moves radially inward at ~ 5 $\mu\text{m s}^{-1}$ toward the axis of the cylindrical sample, the fluorescent probe C-SNARF-1 is rejected by the ice and trapped in the liquid channels, whose morphology depends markedly on the presence of electrolytes (Figure 8.3). C-SNARF-1 in MilliQ water or very dilute electrolyte solutions accumulates into liquid channels arranged in a hexagonal network with well-developed veins, $\delta = (12 \pm 2)$ μm , and nodes occluded in very pure ice (Figure 8.3a). In contrast, C-SNARF is randomly distributed in pockets and dendritic channels, except in the last stages, upon freezing NaCl and $(\text{NH}_4)_2\text{SO}_4$ solutions at concentrations above 1 mM (Figure 8.3b and c). Topological considerations suggest that the average number of sides of the disordered polygonal cells arising spontaneously in systems far from equilibrium via symmetry breaking is six (Figure 8.3a).⁴⁸ We infer that dynamic instabilities, rather than thermodynamics, determine the morphologies observed in our experiments.⁶

Figure 8.4 shows in detail the fluorescence intensity and pH (x, y)-distributions during the freezing of a solution containing 10 μM C-SNARF-1 and 0.1 mM NaCl. Figure 8.4a

shows that the probe was evenly distributed in the sample solution at pH 6.4 across the entire imaging area prior to freezing. As freezing started, C-SNARF-1 was observed to accumulate at the ice front, forming a band of approximately 20 μm in width (Figure 8.4 b), showing that C-SNARF-1 diffusion is slow relative to the forward velocity of the ice front. As shown in Figures 8.4b and c, the pH of the liquid phase increased moderately to ~ 7.2 in the interfacial region and to ~ 7.0 in the bulk liquid away from the interface. pH rose to ~ 8.4 , however, upon thawing the sample after being frozen for 5 minutes (Figure 8.4(d)). The timescales involved are quite consistent with the seepage of OH^- produced at rates: $k_f(\text{H}_2\text{O} \rightarrow \text{H}^+ + \text{OH}^-) = K_w k_b < 10^{-14} \text{ M} \times 10^{10} \text{ M}^{-1} \text{ s}^{-1} = 10^{-4} \text{ s}^{-1}$,⁴⁹ into the pockets, as suggested by Bronshteyn and Chernov.^{29,34,47,50-51} pH returned to the initial value after the sample has completely melted. We verified that the areas under the fluorescence intensity curves (black traces) in Figures 8.4 (c) and (d), along the path $\rho = (x = y)$: $A = \int I(\rho) d\rho$, are identical within experimental error, proving the reversibility of freeze-and-thaw cycles, and indirectly, the absence of self-quenching and other possible artifacts.

Figure 8.5 shows the pH changes during freezing a 0.05 mM $\text{CH}_3\text{COONH}_4$ solution. The pH of the liquid phase was expected to drop during freezing due to preferential incorporation of NH_4^+ into the ice lattice. However, as shown in Figure 8.5 (a) and 8.5 (b), during freezing the pH of the liquid phase slightly increased from approximately 7.9 to 8.2, presumably due to freeze-concentration of an initially basic solution and to the temperature effect. When the sample was thawed after being frozen for 5 minutes, the pH did decrease to 6.8 in the liquids surrounding the air bubbles (Figure 8.5(c)).

8.5 Acknowledgements

This project was financially supported by the National Science Foundation (ATM-0534990).

8.6 Reference

- (1) Duval, P.; Arnaud, L.; Brissaud, O.; Montagnat, M.; de la Chapelle, S. *Ann. Glaciol.* **2000**, *30*, 83.
- (2) Cuffey, K.; Conway, H.; Gades, A.; Hallet, B.; Raymond, C.; Whitlow, S. J. *Geophys. Res.* **2000**, *105*, 27895.
- (3) Cullen, D.; Baker, I. J. *Glaciol.* **2000**, *46*, 703.
- (4) Coriell, S. R.; McFadden, G. B.; Sekerka, R. F. *Annu. Rev. Mater. Sci.* **1985**, *15*, 119.
- (5) Nagashima, K.; Furukawa, Y. *J. Phys. Chem. B* **1997**, *101*, 6174.
- (6) Wettlaufer, J. S. *Europhys. Lett.* **1992**, *19*, 337.
- (7) Brader, J. M.; Voigtmann, T.; Fuchs, M.; Larson, R. G.; Cates, M. E. *Proc. Natl. Acad. Sci. U. S. A.* **2009**, *106*, 15186.
- (8) Cates, M. E.; Wittmer, J. P.; Bouchaud, J. P.; Claudin, P. *Phys. Rev. Lett.* **1998**, *81*, 1841.
- (9) Lu, K.; Brodsky, E. E.; Kavehpour, H. P. *Nat. Phys.* **2008**, *4*, 404.
- (10) Smart, A.; Ottino, J. M. *Soft Matter* **2008**, *4*, 2125.
- (11) Grannas, A. M.; Jones, A. E.; Dibb, J.; Ammann, M.; Anastasio, C.; Beine, H. J.; Bergin, M.; Bottenheim, J.; Boxe, C. S.; Carver, G.; Chen, G.; Crawford, J. H.; Domine, F.; Frey, M. M.; Guzman, M. I.; Heard, D. E.; Helmig, D.; Hoffmann, M.

- R.; Honrath, R. E.; Huey, L. G.; Hutterli, M.; Jacobi, H. W.; Klan, P.; Lefer, B.; McConnell, J.; Plane, J.; Sander, R.; Savarino, J.; Shepson, P. B.; Simpson, W. R.; Sodeau, J. R.; von Glasow, R.; Weller, R.; Wolff, E. W.; Zhu, T. *Atmos. Chem. Phys.* **2007**, *7*, 4329.
- (12) Domine, F.; Albert, M.; Huthwelker, T.; Jacobi, H. W.; Kokhanovsky, A. A.; Lehning, M.; Picard, G.; Simpson, W. R. *Atmos. Chem. Phys.* **2008**, *8*, 171.
- (13) Huthwelker, T.; Ammann, M.; Peter, T. *Chem. Rev.* **2006**, *106*, 1375.
- (14) Price, P. B. *FEMS Microbiol. Ecol.* **2007**, *59*, 217.
- (15) Price, P. B.; Rohde, R. A.; Bay, R. C. *Biogeosciences* **2009**, *6*, 479.
- (16) Rohde, R. A.; Price, P. B.; Bay, R. C.; Bramall, N. E. *Proc. Natl. Acad. Sci. U. S. A.* **2008**, *105*, 8667.
- (17) Dash, J. G.; Rempel, A. W.; Wettlaufer, J. S. *Rev. Mod. Phys.* **2006**, *78*, 695.
- (18) Benatov, L.; Wettlaufer, J. S. *Phys. Rev. E* **2004**, *70*.
- (19) Mader, H. M. *J. Glaciol.* **1992**, *38*, 333.
- (20) Mader, H. M. *J. Glaciol.* **1992**, *38*, 359.
- (21) Nye, J. F. *J. Glaciol.* **1989**, *35*, 17.
- (22) Workman, E. J.; Reynolds, S. E. *Phys. Rev.* **1950**, *78*, 254.
- (23) Cobb, A. W.; Gross, G. W. *J. Electrochem. Soc.* **1969**, *116*, 796.
- (24) Gross, G. W. *Adv. Chem. Ser.* **1968**, *27*.
- (25) Grimm, R. E.; Stillman, D. E.; Dec, S. F.; Bullock, M. A. *J. Phys. Chem. B* **2008**, *112*, 15382.
- (26) Gross, G. W.; Wong, P. M.; Humes, K. J. *Chem. Phys.* **1977**, *67*, 5264.

- (27) O'Driscoll, P.; Minogue, N.; Takenaka, N.; Sodeau, J. *J. Phys. Chem. A* **2008**, *112*, 1677.
- (28) Takenaka, N.; Ueda, A.; Maeda, Y. *Nature* **1992**, *358*, 736.
- (29) Takenaka, N.; Tanaka, M.; Okitsu, K.; Bandow, H. *J. Phys. Chem. A* **2006**, *110*, 10628.
- (30) Takenaka, N.; Bandow, H. *J. Phys. Chem. A* **2007**, *111*, 8780.
- (31) Sato, K.; Furuya, S.; Takenaka, N.; Bandow, H.; Maeda, Y.; Furukawa, Y. *Bull. Chem. Soc. Jpn.* **2003**, *76*, 1139.
- (32) Sato, K.; Takenaka, N.; Bandow, H.; Maeda, Y. *J. Phys. Chem. A* **2008**, *112*, 7600.
- (33) Takenaka, N.; Furuya, S.; Sato, K.; Bandow, H.; Maeda, Y.; Furukawa, Y. *Int. J. Chem. Kinet.* **2003**, *35*, 198.
- (34) Takenaka, N.; Ueda, A.; Daimon, T.; Bandow, H.; Dohmaru, T.; Maeda, Y. *J. Phys. Chem.* **1996**, *100*, 13874.
- (35) Wettlaufer, J. S.; Worster, M. G. *Ann. Rev. Fluid Mech.* **2006**, *38*, 427.
- (36) Sadtchenko, V.; Ewing, G. E. *J. Chem. Phys.* **2002**, *116*, 4686.
- (37) Wei, X.; PB, M.; C, Z.; Shen, Y. R. *Phys. Rev. B* **2002**, *66*, art. no.
- (38) Wei, X.; Miranda, P. B.; Shen, Y. R. *Phys. Rev. Lett.* **2001**, *86*, 1554.
- (39) Doppenschmidt, A.; Butt, H.-J. *Langmuir* **2000**, *16*, 6709.
- (40) Barnes, P. R. F.; Wolff, E. W. *J. Glaciol.* **2004**, *50*, 311.
- (41) Barnes, P. R. F.; Wolff, E. W.; Mallard, D. C.; Mader, H. M. *Microsc. Res. Tech.* **2003**, *62*, 62.

- (42) Baker, I.; Iliescu, D.; Obbard, R.; Chang, H.; Bostick, B.; Daghljan, C. P. Microstructural characterization of ice cores. In *Ann. Glaciol.*; Dowdeswell, J., Willis, I. C., eds., 2005; vol. 42; pp 441.
- (43) Rempel, A. W.; Waddington, E. D.; Wettlaufer, J. S.; Worster, M. G. *Nature* **2001**, *411*, 568.
- (44) Hobbs, P. V. *Ice Physics*; Clarendon Press: Oxford, 1974.
- (45) Pawley, J. B. *Handbook of Biological Confocal Microscopy*, 2nd ed.; Plenum Press: New York, 1995.
- (46) Mason, W. T. *Fluorescent and Luminescent Probes for Biological Activity*, 2nd ed.; Academic Press: London, U.K., 1999.
- (47) Robinson, C.; Boxe, C. S.; Guzman, M. I.; Colussi, A. J.; Hoffmann, M. R. *J. Phys. Chem. B* **2006**, *110*, 7613.
- (48) Schliecker, G. *Adv. Phys.* **2002**, *51*, 1319.
- (49) Geissler, P. L.; Dellago, C.; Chandler, D.; Hutter, J.; Parrinello, M. *Science* **2001**, *291*, 2121.
- (50) Bronshteyn, V. L.; Chernov, A. A. *J. Cryst. Growth* **1991**, *112*, 129.
- (51) Sola, M. I.; Corti, H. R. *An. Asoc. Quim. Argent.* **1993**, *81*, 483.

Table 8.1. Fitting parameters of equation (8.2) obtained under various temperature and instrument conditions.

Instrument	T (k)	$\lambda_1(\text{nm})$	$\lambda_2(\text{nm})$	c	R_{\min}	R_{\max}	$\log \frac{I^a}{I^b}$
FL	298	587	634	-1.089	0.078	2.184	-0.425
CLSM	298	581	635	-1.119	0.095	2.413	-0.321
CLSM	288	581	635	-1.144	0.095	2.409	-0.229
CLSM	278	581	635	-1.145	0.099	2.379	-0.114
CLSM	268	581	635	-1.148	0.100	2.360	0.005

Figure 8.1. A typical temperature profile during the freeze-thaw cycle of electrolyte solution sample. Red line: cryostage programmed temperature. Black line: actual sample temperature.

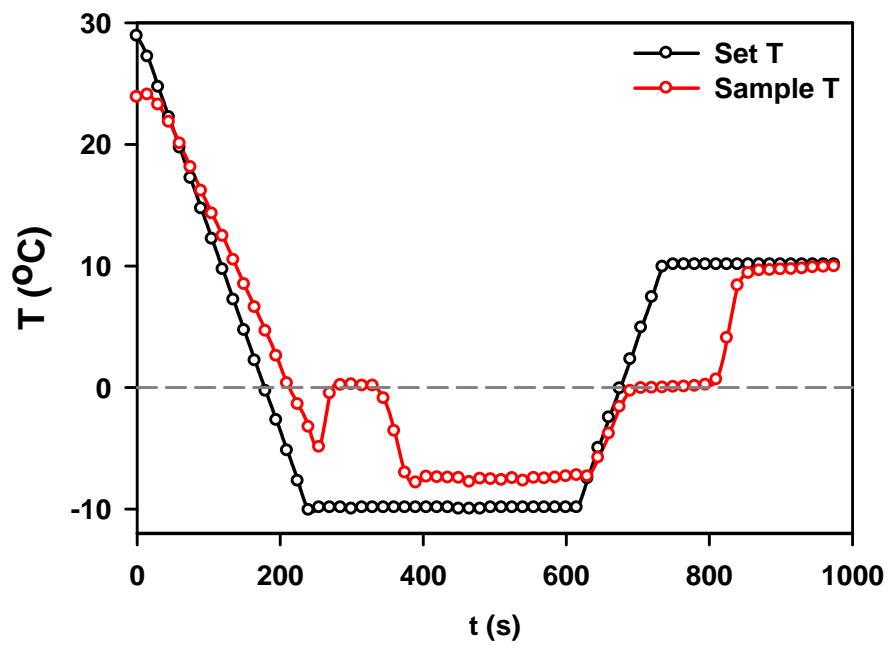


Figure 8.2. Fluorescence emission ratio vs. pH measured by fluorometer (FL, blue line; $\lambda_1 = 587$ nm, $\lambda_2 = 634$ nm) and by CLSM (red line; $\lambda_1 = 581$ nm, $\lambda_2 = 635$ nm). The solutions measured by fluorometer experiments contain 0.2 μ M C-SNARF-1 and 0.05 M $\text{KH}_2\text{PO}_4/\text{K}_2\text{HPO}_4$ buffer, and those measured by CLSM contain 1.0 μ M C-SNARF-1 and 0.05 M phosphate buffer.

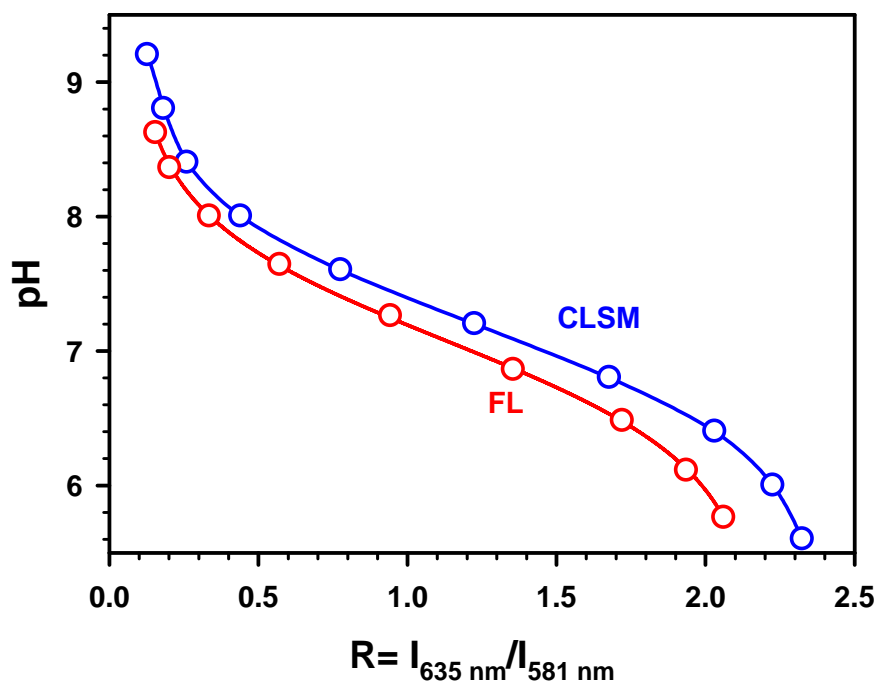
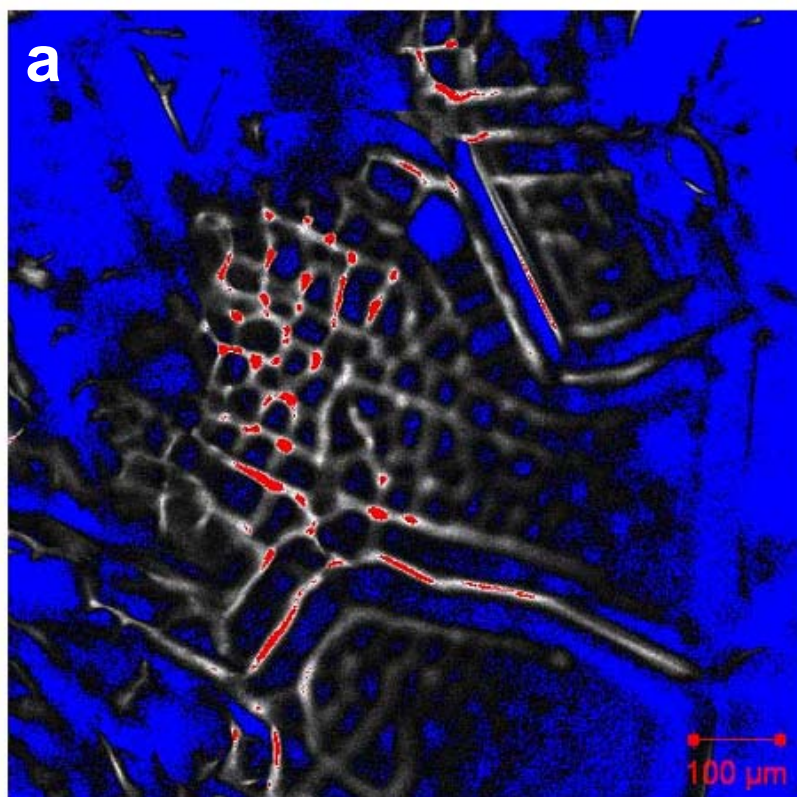


Figure 8.3. 10 μM C-SNARF-1 in (a) MilliQ, (b) 1mM NaCl solution, (c) 1mM $(\text{NH}_4)_2\text{SO}_4$ solution during freezing. Fluorescence intensity is indicated by a color scale (blue: zero-low intensity, red: high intensity-saturation). Frame sizes are $900\ \mu\text{m} \times 900\ \mu\text{m}$ for (a) and $225\ \mu\text{m} \times 225\ \mu\text{m}$ for (b) (c).



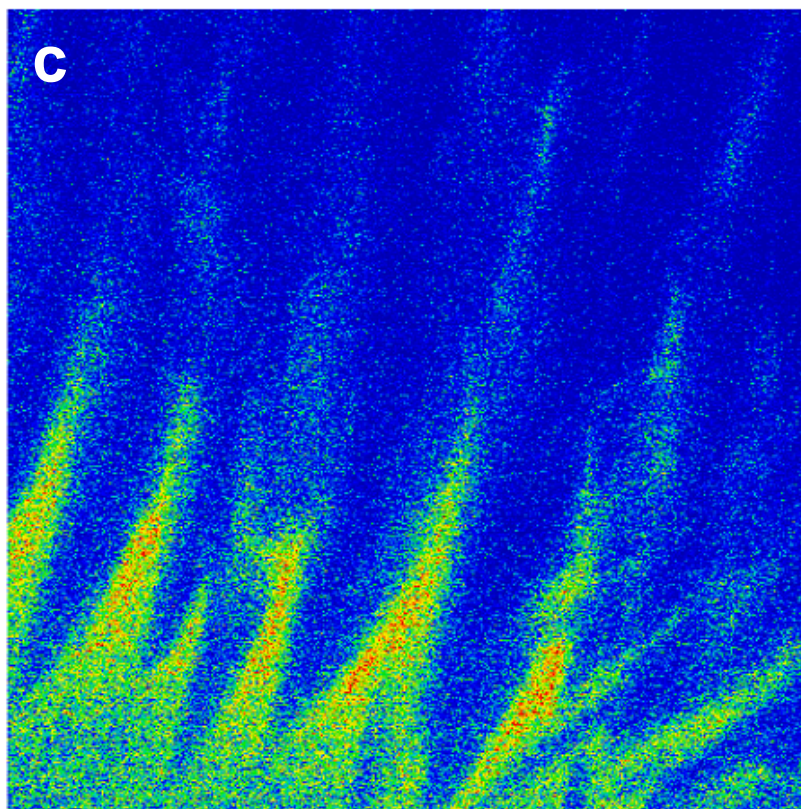
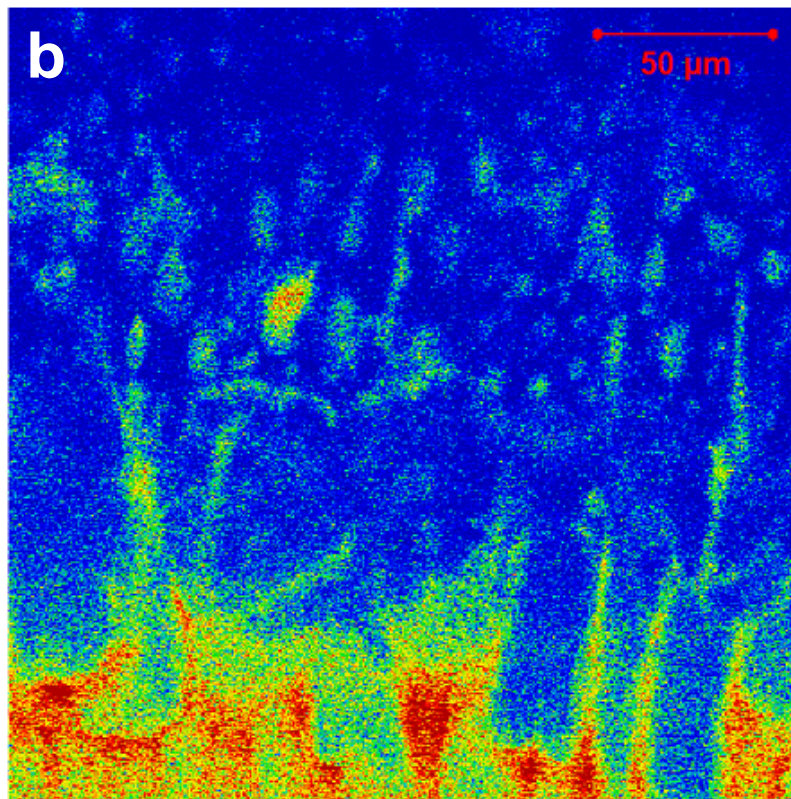
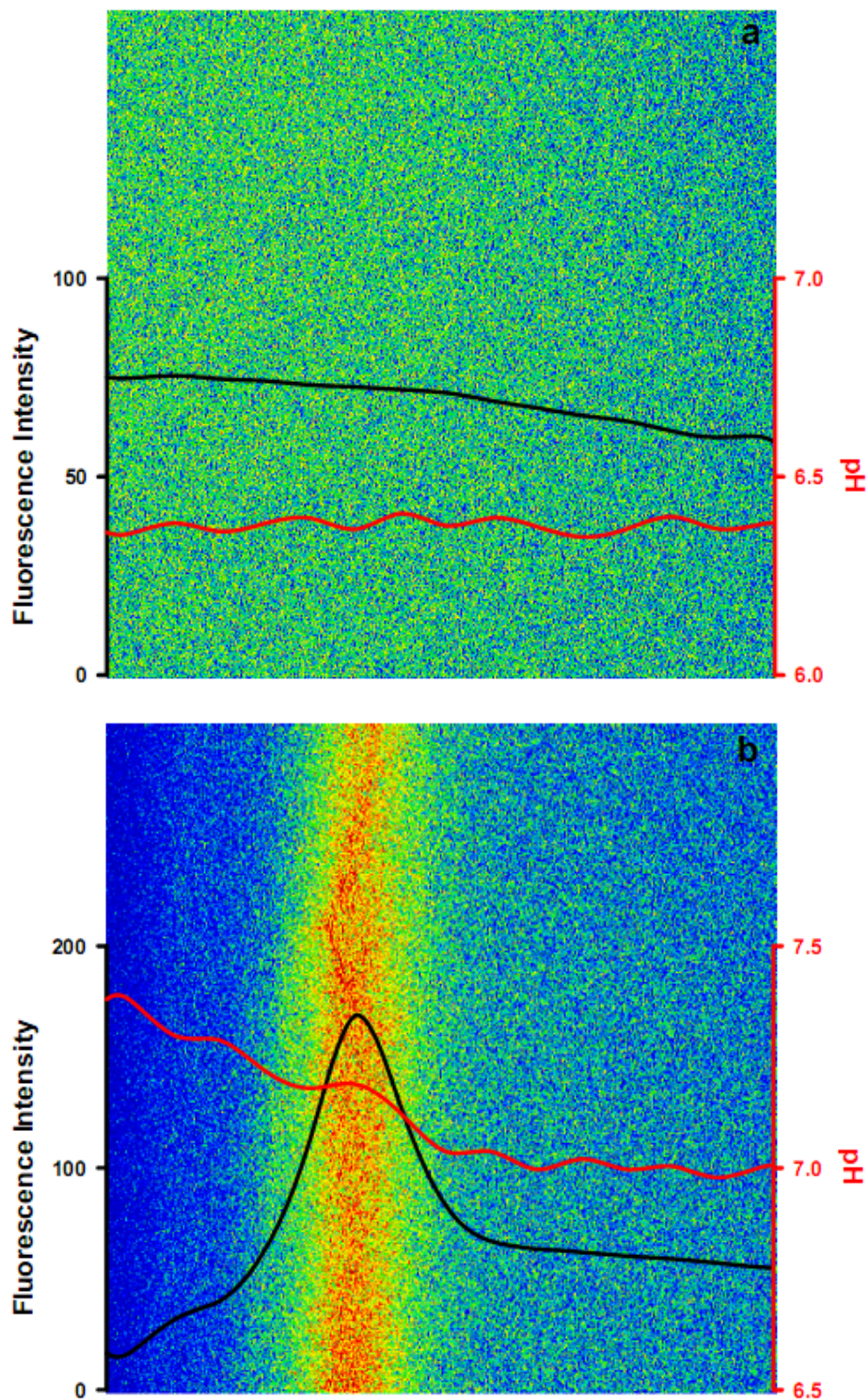


Figure 8.4 Fluorescence emission spectra of an aqueous solution containing 10 μM C-SNARF-1 and 0.1 mM NaCl (a) before freezing, (b) 9.8s after freezing began, (c) 52.4 s after freezing began, and (d) 20 s after thawing began. The pH values shown are based on the emission ratio averaged over the area of interest. The frame size is $225 \mu\text{m} \times 225 \mu\text{m}$.



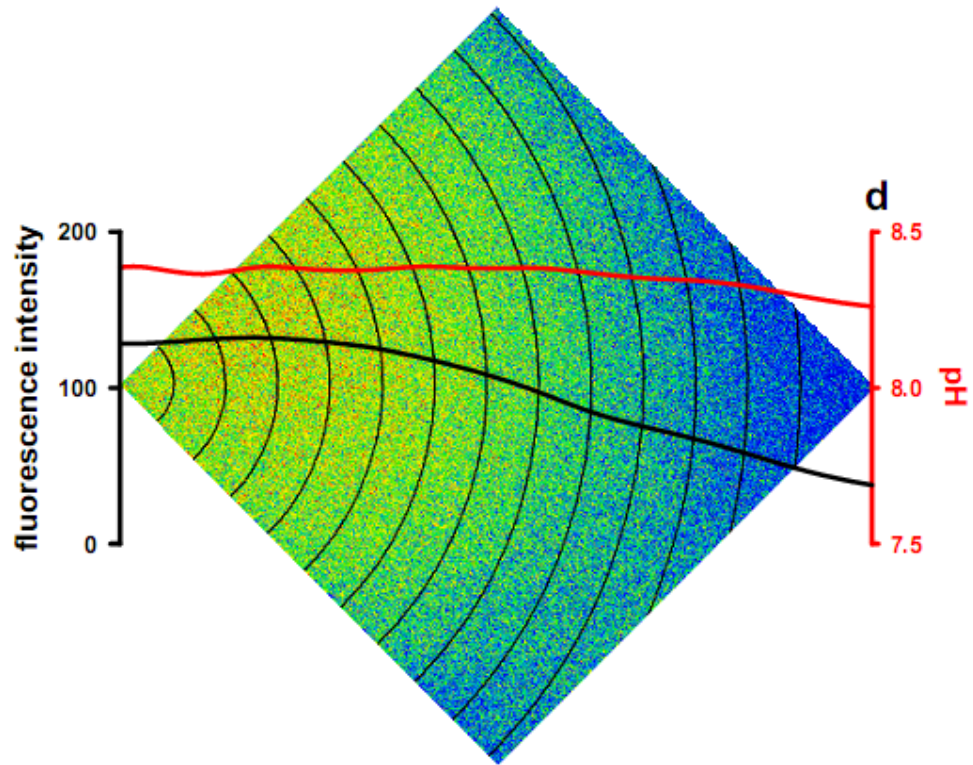
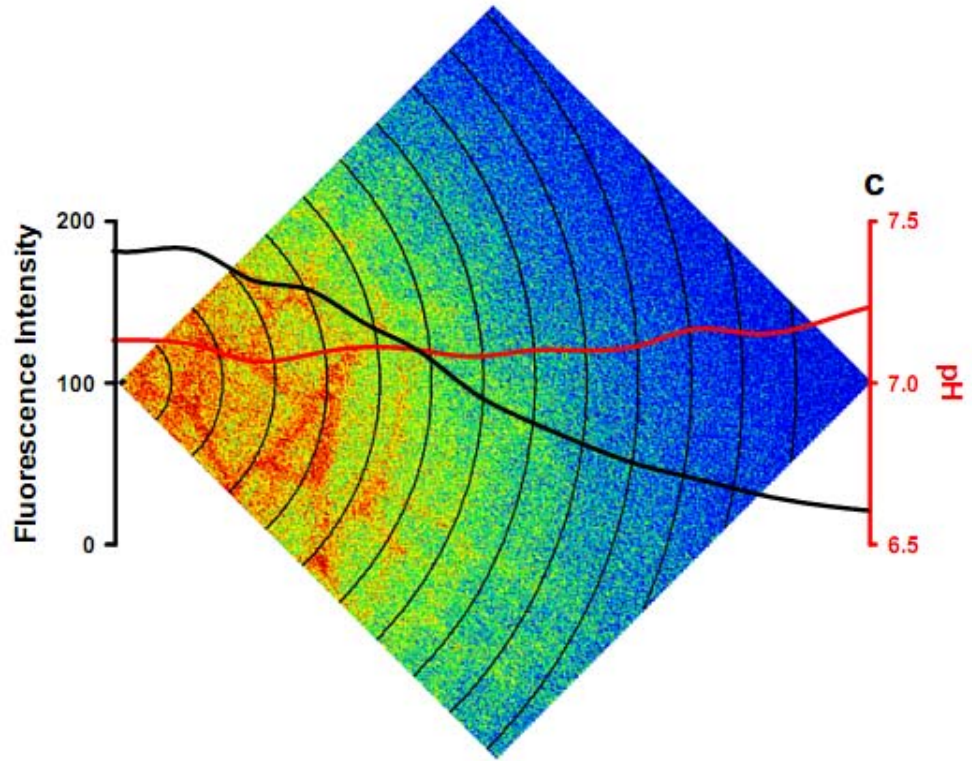
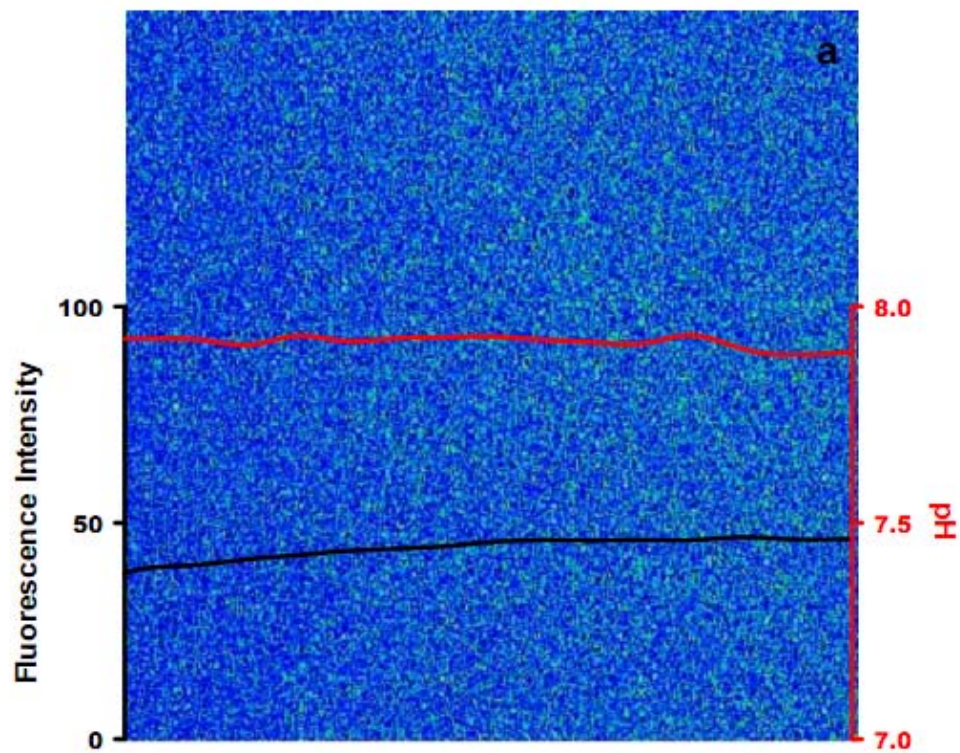


Figure 8.5. Fluorescence emission spectra of an aqueous solution containing 5 μM C-SNARF-1 and 0.05 mM $\text{CH}_3\text{COONH}_4$ (a) before freezing at 298 K, (b) during freezing, and (c) during thawing. The pH values shown are based on the emission ratio averaged over the area of interest. The frame size is 225 $\mu\text{m} \times 225 \mu\text{m}$.



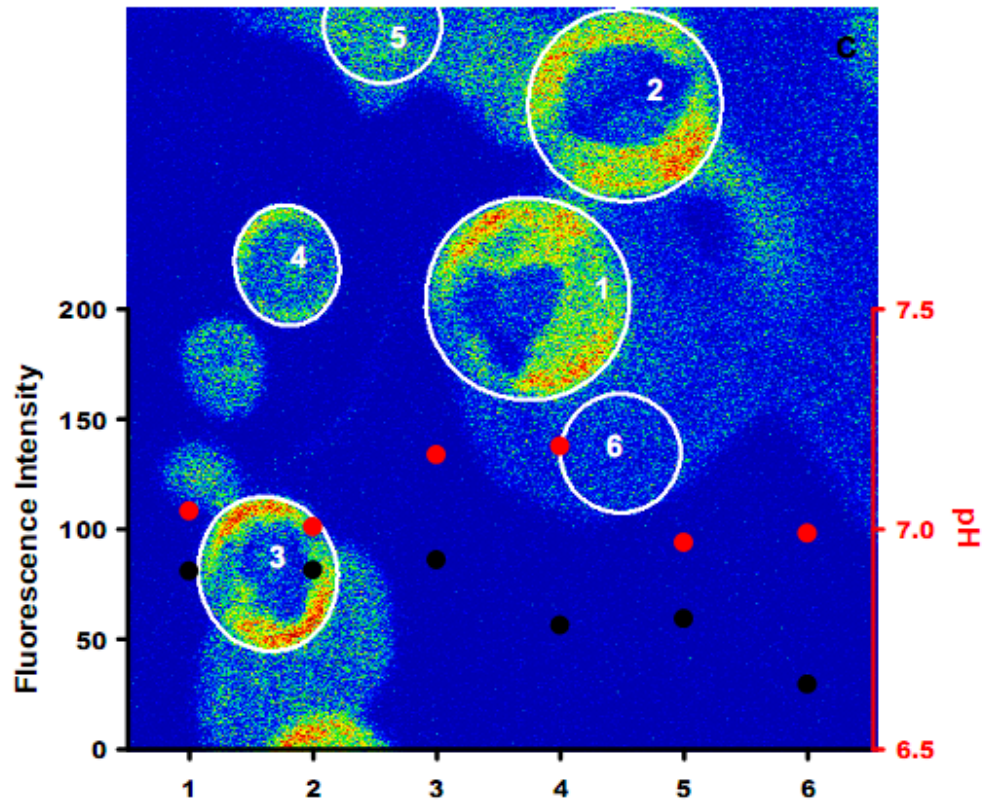
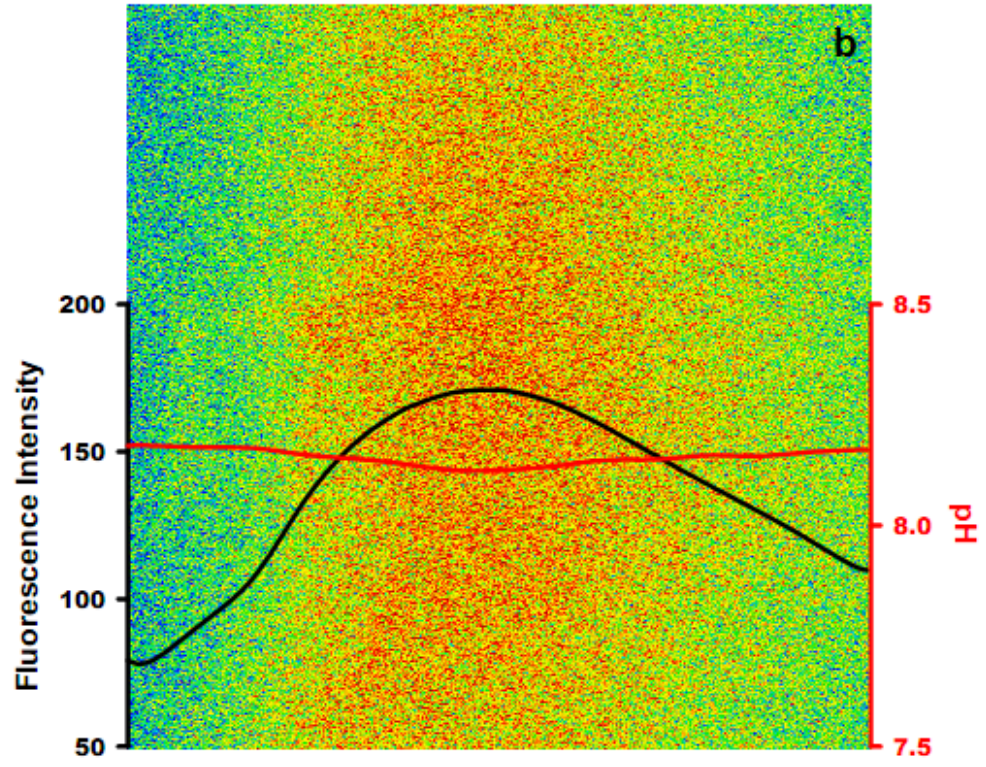


Figure 8.6. fluorescence emission ratio vs. pH measured by CLSM at different temperatures. The solutions contain 1.0 μM C-SNARF-1 and 0.05 M phosphate buffer.

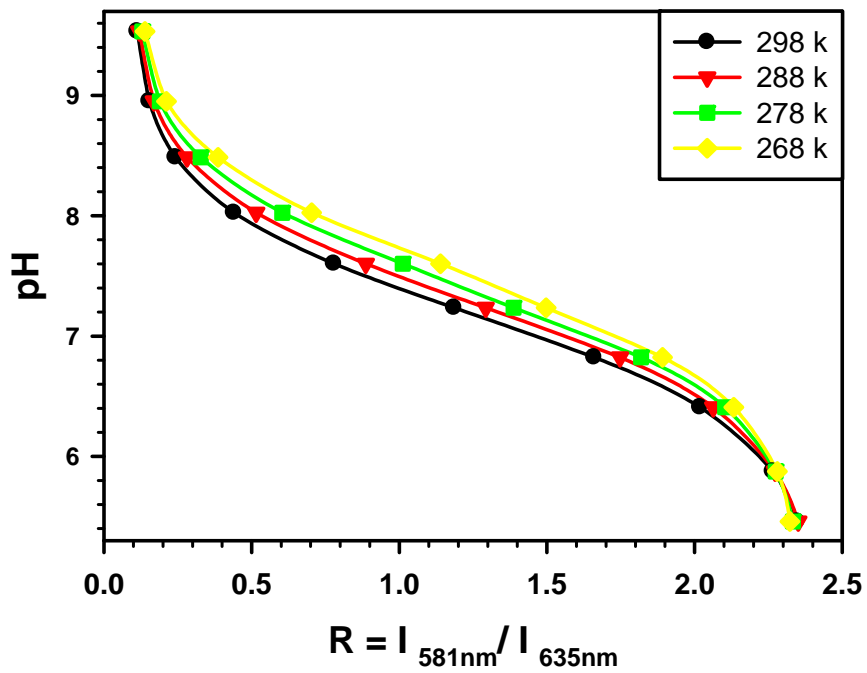


Figure 8.7. fluorescence emission ratio measured by CLSM as a function of (a) laser intensity and (b) C-SNARF-1 concentration.

